Soft Matter

Accepted Manuscript

This article can be cited before page numbers have been issued, to do this please use: S. Chen, H. Zhang, Z. Guo, I. Pagonabarraga and X. Zhang, *Soft Matter*, 2026, DOI: 10.1039/D6SM00300A.

ROYAL SOCIETY OF CHEMISTRY

rsc.li/soft-matter-journal

View Article Online
DOI: 10.1039/D6SM00300A

Plug flow down to nanoscale can induce partial solidification of confined fluids

Shan Chen,[a] Hongguang Zhang,[b] Zhenjiang Guo,[c] Ignacio Pagonabarraga[d,e,*] and Xianren Zhang[c,*]

[a] College of Traditional Chinese Medicine, Bozhou University, Bozhou 236800, China

[b] Clinical Research Institute of Clinical Medicine, Nanjing Drum Tower Hospital, Medical School, Nanjing University, Nanjing 210093, China

[c] State Key Laboratory of Organic-Inorganic Composites, Beijing University of Chemical Technology, Beijing 100029, China

[d] Department of Condensed Matter Physics, Faculty of Physics, University of Barcelona, C. Martí i Franquès 1, E08028 Barcelona, Spain

[e] UBICS University of Barcelona Institute of Complex Systems, Martí i Franquès 1, E08028 Barcelona, Spain

* E-mail address: zhangxr@mail.buct.edu.cn (X. Z.), ipagonabarraga@ub.edu (I. P.)

Abstract

In this work we employ molecular dynamics simulation to study the anomalous fluid behavior of plug nanoflow. We find that the simultaneous use of plugging and nano-confinement suppresses the ability of fluid to flow, leading to molecular clogging. Our simulations demonstrate that molecular clogging enhances the fluid/solid friction in a non-linear manner and leads to various novel flow patterns. Our analysis reveals that the non-monotonic friction behavior is a consequence of the sudden transition for the confined fluid from liquid state to partial solid-like state when the pore size decreases. The partial solidification is featured with piecewise response of the liquid velocity, pressure, and density distributions. The solidification in fact originates from the combined action between clogging and interfacial friction: clogging increases friction, inducing an enhanced internal compression of the confined liquid that causes partial solidification. The driving mode also critically alters the flow patterns: constant-velocity driving yields piecewise flow profiles, while constant-force driving triggers abrupt stick–slip transitions in small pores where

View Article Online
DOI: 10.1039/D6SM00300A

solidification occurs. Our findings challenge the traditional view of confined fluids as homogeneous liquids and establish a compression-based mechanism linking interfacial friction, molecular clogging, and flow-induced solidification.

View Article Online
DOI: 10.1039/D6SM00300A

1 Introduction

The structure and dynamics of confined liquids are essential for their potential applications in microfluidics and nanofluidics.[1-3] However, the new challenge is that, as the confined liquid scales down to the nanoscale, the flow behavior observed often shows qualitative deviations from bulk expectations.[4] A pertinent example is the lubrication at the nanoscale. The friction properties of confined liquids are found to depend strongly on the confinement and morphologies of lubricant molecules.[5-7] Yet, how lubricant molecules organize under strong confinement remains unclear. Even for a much simpler model lubricant system, *i.e.*, simple liquid is confined between two atomically smooth surfaces, fundamental questions regarding the phase behavior and shear properties are still in debate.[8-17]

Since such model systems can be realistically simulated using molecular dynamics (MD) simulations, MD has emerged as an important tool capable of providing insight into the working mechanism of lubricants. Although real systems are more complex, the use of simple models in molecular simulations have elucidated the appearance of a liquid to solid-like phase transition when the width between two atomically smooth surfaces drops below a certain value.[18-21] In our previous work, we investigated a particular regime of liquid lubrication called mixed lubrication, which can be modeled with plug-like nanoflows at the nanoscale.[22] We found that the presence of solid-solid contacts not only induces solid-solid friction but also leads to so-called molecular clogging, which substantially changes the lubricant flow behavior and leads to enhanced liquid/solid friction. The term of molecular clogging was introduced to describe a kinetic hindrance effect specific to strongly confined molecular fluids under plug-flow conditions.

Following our previous work, in this study we systematically studied the flow structures of plug nanoflows observed within a large range of pore size. We firstly find a non-monotonic friction–pore size relationship that was absent in our previous work. Secondly, we reveal that molecular clogging can, under sufficiently strong confinement, induce a local liquid-to-solid-like transition, which fundamentally alters the mechanical response of the confined flow. This partial solidification is then confirmed with various structural and dynamical characteristics. Third, we compare constant-velocity and constant-force driving, uncovering qualitatively different kinetic responses. These findings not only extend our earlier work but also challenge classical continuum predictions and open a new direction for understanding nanoscale friction as a flow-induced non-equilibrium phase behavior.

2 Models and simulation method

To understand the friction force between encaged nanofluids and their confining substrates, we consider a molecular liquid confined in a slit pore, nanometric in size, composed of two parallel solid substrates (see Fig. 1). A driving solid piston, which moves either at a prescribed constant

View Article Online
DOI: 10.1039/D6SM00300A

velocity U or at a constant force *F*, is placed on the left to push the liquid column to create the plug nanoflow, and the right piston at the right end of liquid slab can move freely to eliminate the capillary force. As shown in our previous work,[18] the presence of the pistons, especially the driving piston, inhibits the internal flow of the liquid column and changes the flow structure, giving rise to an important effect called molecular clogging. To separate the solid-liquid friction from the solid-solid friction, the interaction between pistons and solid substrate was set to zero.

We need to stress that in our simulation, the driving piston is designed to generate plug-like flow and molecular clogging. In real nanoscale friction or lubrication systems, a similar relative motion between a confined fluid and its confining surfaces (e.g., a sliding asperity or a moving substrate) can induce an analogous effect: the local suppression of internal flow could potentially leading to partial solidification. Thus, the key physical phenomenon is not the piston itself, but the combination of extreme confinement and relative motion that produces a localized, friction-induced compression strong enough to trigger a liquid-to-solid-like transition, as shown below.

By employing Molecular Massively Parallel Simulator (LAMMPS)[23] we have simulated the resulting liquid/solid friction by the plug nanoflow as a function of the confinement, which is represented by the inter-substrate distance. In our simulations, the non-bonded interaction, $U_{ij}(r)$, between any two atoms of type i and j is represented by the 12-6 Lennard-Jones (LJ) potential

$$U_{ij}(r) = 4\varepsilon_{ij}\left[\left(\frac{\sigma_{ij}}{r}\right)^{12} - \left(\frac{\sigma_{ij}}{r}\right)^{6}\right] \quad (1)$$

where r is the distance between the beads, σ_{ij} is the size parameter, and ε_{ij} is the energy parameter. Here, i and j can refer to atoms of wall (w), piston (p), and liquid (l). All variables in our simulation are expressed in units of the interaction between liquid atoms, with length and energy scales denoted as $\sigma = \sigma_{ll}$ and $\varepsilon = \varepsilon_{ll}$. For the LJ potential the cutoff radius r_c was set to 2.5σ. Here we adopted a coarse-grained chain model as a minimal representation of lubricants, in which each lubricant molecule is modeled by chain-like LJ molecules, each containing eight LJ beads. The intramolecular bonded interactions of the chain-like molecules are modelled by a finite extensible nonlinear elastic (FENE) potential[24]

$$E = -\frac{1}{2}kr_0^2\ln\left[1-\left(\frac{r_{bond}}{r_0}\right)^2\right] \quad (2)$$

Standard values for the bead-spring polymer model[25-27], namely the FENE spring constant $k = 30\epsilon/\sigma^2$ and maximum extension $r_0 = 1.5\sigma$, were used here. To simplify the description, we used LJ units. For the unit conversion, the LJ particles can be considered as argon atoms, *i.e.*, $\sigma = 3.41$Å, $m = 6.64 \times 10^{-26}$kg and $\varepsilon = 10.30$meV.[28]

View Article Online
DOI: 10.1039/D6SM00300A

The size of the quasi-two-dimensional simulation box is set to $15 \times 200 \times (H + 36)$, with H the distance measured from the centers of the solid atoms in the innermost substrate layers (Fig. 1). Periodic boundary conditions are applied in all three directions, while the simulation box extends its size in the Z direction that is 28 larger than the pore size, in order to minimize the effect of periodic boundary condition. The liquid slab contains $120 \times (H-1)$ liquid molecules with an initial length of 64. The wettability of two confining substrates is ensured to be hydrophilic by setting $\varepsilon_{lw} = 0.8$, corresponding to a contact angle of 52°, while the pistons are almost neutral ($\varepsilon_{lp} = 0.6$ with a contact angle of 86°).[22]

Both the pistons and the walls are assumed to be rigid, namely the solid atoms are fixed at their lattice sites without thermal motion. NVT is used for the liquid (see Fig. 1) to update atom positions and velocities at each time step. The classic velocity Verlet algorithm[29] is used for the integration of equations of motion, and a Nosé–Hoover thermostat[30,31] is used to maintain the liquid temperature to $T = 0.8$ in reduced units. In our simulation runs, typically 5.2ns are required to reach the steady state, followed by a production time interval, up to 32ns, to obtain the friction and flow characteristics. The friction force is computed as the sum of all lateral forces in the flow direction exerted by the confining substrates on the liquid beads, and this value is averaged over the production interval.

3 Results and discussion

In this work, we considered two distinct strategies for moving the driving piston: applying a constant velocity or applying a constant force to the driving piston. We found that due to the molecular clogging at small pore sizes, constant velocity and constant force scenarios both exhibit partial solidification as well as solidification-triggered friction reduction, but differ in how they trigger and respond to phase transitions. To simplify the description, we considered first the constant velocity scenario, and then described the constant force scenario in the last section as a comparison.

3.1 The constant velocity scenario: the solidification inside small pores and non-monotonous effect of pore width on friction

The non-monotonous dependence of friction force on the pore width. We first consider the effect of confinement on the resulting friction between the plug flow and the confining substrates. To this end, we vary the inter-substrate distance, H, from 5 to 200. At a given distance between the two confining walls, a constant velocity $U = 0.015$ (in reduced units) along the Y direction was applied to the driving piston on the left of the liquid slab, which forces the liquid slab to move at the same average velocity. After the liquid slab reached the steady state, we output the friction forces exerted on the liquid slab by the confining substrates, F_f, as well as the driving force

View Article Online
DOI: 10.1039/D6SM00300A

exerted by the pistons, F^e, every 0.0065ns. By averaging the forces, we indeed find, $F^e = F_f$, indicating that force balance is reached.

Fig. 2 displays the measured friction force as a function of the pore width. It shows that a significantly enhanced friction is generated for plug nanoflow, especially when the pore size decreases to several molecular size. More interestingly, the figure clearly shows a non-linear and non-monotonous relationship between the friction force and the pore width. When pore width is rather small, in the range of 5 to 7, the friction force decreases sharply with the increase of the pore width. As the pore width increases from $H = 7$ to 8, however, the friction force displays, on the contrary, a steep increase. Further increasing the pore size again leads to a decrease of the frictional force. Finally, for $H > 50$, the friction force remains constant when the pore size continues to increase.

We have considered the impact of U on the friction force, through comparing to the resulting friction at a smaller piston velocity of $U = 0.0075$ (Fig. 2b). The figure shows that a smaller velocity generally leads to a decreased friction. But a similar and non-monotonous dependence of friction force on the pore width is found, irrespective of the magnitude of the piston velocity, U. The non-monotonous behavior observed indicates that there exist two different mechanisms governing the relationship between friction force and pore width. Moreover, for the relatively small pore widths ($H \leq 7$), the driving velocity basically does not change the friction force, as shown in Fig. 2b. For larger pore widths, however, the decrease of the driving velocity, U, would significantly decrease the induced friction. Below we will explain the complex friction-velocity relationship.

The molecular clogging effect as a function of pore size. The enhanced friction displayed in Fig. 2 can be interpreted in terms of molecular clogging.[18] The presence of the pistons, especially the driving piston, as well as the confining walls, inhibits the internal flow of the confined liquid and changes the flow pattern, giving rise to an important effect called molecular clogging. This effect will be further illustrated here.

The clogging effect is a joint consequence of the confinement (represented by inter-substrate distance) and the presence of the pistons, both of which suppresses the ability of fluid to flow, cooperatively hinder the internal motion of the liquid and enhance the friction on solid interfaces. First, the pistons play an essential role in initiating the clogging effect, since their presence enables the confined liquid to resist a large interfacial friction. Second, confinement affects significantly clogging, which can be recognized by the nanoflow velocity profile that is shown below.

We have analyzed the averaged velocity profile of the plug nanoflow, $V(y,z)$. To this end, we divided the liquid into several bins, each with dimensions of $1\sigma \times 5\sigma$ along Z and Y axis, respectively. We found that this binning is enough to obtain the relative velocity profile and ensuring to get

View Article Online
DOI: 10.1039/D6SM00300A

enough statistics by summing up over 10^5 configurations. Here *y* and *z* denote the relative position of each small cell in the liquid slab in relation to the position of the driving piston. The profile of the relative velocity, with respect to the driving piston, is then determined by setting $V_{relative}(y,z) = V(y,z) - U$. As shown in Fig. 3, the relative velocity profile for the liquid slab shows three different trends, depending on the levels of spatial confinement.

We first discuss the situations of large pores, e.g., for $H = 19$ (see Fig. 3d). The figure shows a typical flow pattern that was revealed in our previous work[22]: two loops of the friction-driven circulations can be identified. The relative motion appears near the liquid/substrate interfaces, which is accompanied by a smaller forward flow in the center of channel that cancels off backward motion of the liquid molecules on the interface. This kind of flow pattern induces an enhanced friction because the friction takes place along the whole liquid-substrate interface, rather than being localized in the vicinity of the contact line as it is commonly expected for macroscopic flows.

When the pore size is decreased to $H = 8$, however, the relative velocity changes qualitatively, showing a piecewise flow pattern (see Fig. 3c). The new flow pattern can be understood as a combination of two different parts, each having different dynamic features. For the part near the driving piston, the flow shows a signal of solid/solid friction: nearly zero relative velocity with respect to the motion of the driving piston, namely the disappearance of the internal flow. However, a distinguishable slip velocity along the interface is found, indicating that there exists a molecular layer that remains in a liquid-like state nearby each confining substrate. The remaining part that locates far from the driving piston shows a relative larger velocity profile along the interface, and more importantly clearer vortices can be identified (similar to the friction-driven circulations observed for $H = 19$). The comparison between the flows for $H = 19$ and $H = 8$ demonstrates that as pore size decreases, the circulation motion is severely suppressed particularly for the part near the piston, enhancing clogging. More importantly, a piecewise flow structure develops when the pore size decreases to $H = 8$.

When pore size is further reduced to 7 and 5 (see Fig. 3b and 3a, respectively), the piecewise profile for the relative velocity becomes more evident. In the region close to the driving piston, the relative velocity along the Y axis is basically zero, i.e. with the same velocity as that of the driving piston. This observation, along with the pressure and density profiles that discussed below (Fig. 4 and Fig. 5), proves the solid-like structure for the part of encaged liquid near the driving piston. Out of the solidified region, the relative velocity for the liquid is characterized by a forward flow in the center of channel, which is canceled off by the backward motion along the interface.

In general, the different flow patterns observed in Fig. 3 are a consequence of the clogging effect, which is induced by the presence of the driving piston and is enhanced by the confinement, both of which cooperatively hinder the relative liquid motion and leads to enhanced friction. For

View Article Online
DOI: 10.1039/D6SM00300A

relatively large pores, clogging can be weakened by internal motion inside the liquid slab, and the formation of vortices compensates for the interfacial friction.[18] But for rather small pore size, the clogging effect becomes severe, and the piecewise flow pattern appears instead, as a signal of partial solidification.

Now, we re-interpret the term of molecular clogging that we introduced previously.[18] In classical hydrodynamics, a fluid is defined by its ability to flow continuously under an applied shear stress. However, in the present system, the combination of extreme confinement and strong interfacial friction produces a local stress state that arrests internal motion. Thus, the conventional notion of a fluid as a homogeneous, flowing medium breaks down under these extreme conditions. Instead, the system becomes spatially partitioned into a solid-like clogged zone and a liquid-like flowing zone. We propose that molecular clogging serves as the key criterion for this transition: when the pore size is sufficiently small, the fluid locally loses its fluidity and the molecular clogging takes place as the key mechanistic link between confinement, friction, and solidification. This clogging effect is distinct from equilibrium jamming in that it is driven by external forcing and occurs at molecular scales under non-equilibrium steady-state conditions.

Partial solidification is a consequence of the liquid compression induced by interfacial friction.

The simulations show that inside a rather small pore ($H < 8$), the liquid column is partially solidified: the part near the driving piston is solidified whereas the rest remains in a liquid-like state. Analyzing the distribution of the pressure tensor along the liquid column, we demonstrate that partial solidification is due to the compression associated to the strong interfacial friction: When the liquid column is subject to quasi-static friction along the interface, the presence of clogging causes the interfacial friction to produce an internal compression of the confined liquid, and therefore the pressure tensor increases along the liquid column.

Fig. 4 displays the distribution of the pressure tensor (p_{zz}) along the Z axis to analyze the internal pressure of the confining fluid caused by the driving piston. For determining the pressure component p_{zz}, we followed the mechanical route[32] as described by Shi et al. As a comparison, Fig. 4a and b depict p_{zz} for the confined liquid column in equilibrium (without applying a driving velocity by setting $U = 0$). The figures show that p_{zz} of the liquid slab is evenly distributed along the Y axis; Along the Z axis, the pressure tensor of liquid slab has two large peaks near the solid walls. This is expected due to the attractive force from the hydrophilic confining substrates, which results in packing of the liquid molecules in the vicinity of the substrates. From the substrates to the middle of the pore, p_{zz} gradually decays but still several small peaks appear, which is the

View Article Online
DOI: 10.1039/D6SM00300A

well-known layer-like liquid structure due to strong spatial confinement.

When a constant velocity, $U = 0.015$, is applied to the driving piston, however, the profile of pressure tensor substantially changes (see Fig. 4c-f). For $H = 5$ (Fig. 4c) and $H = 7$ (Fig. 4d), the pressure tensor component p_{zz} significantly increases, and a piecewise distribution appears again, similarly to the behavior observed for the velocity distribution (Fig. 3a and b). For the part of the liquid slab far away from the driving piston, the pressure tensor component p_{zz} increases sharply along the direction towards the driving piston. The generated pressure gradient is due to the combined action between clogging and interfacial friction: clogging increases the friction, and the friction along with the clogging effect induces the strong internal compression effect along the liquid slab. Therefore, the superposition of the compression along the direction towards the driving piston increases the internal liquid pressure quite quickly, until a plateau is reached. The plateau in the pressure tensor component p_{zz}, which appears in the region with $V_{relative}(y,z) \approx 0$ in Fig. 2, is a signal of solidification. Therefore, the pressure tensor component p_{zz} shows that the second part of the liquid slab, which is close to the driving piston, is in fact in a solid state. This is why the pressure in this part does not change substantially along the interface, since the superposition effect would vanish once the compressed liquid is solidified.

The obtained profile of the pressure tensor rationalizes the non-monotonous relation between the friction and the pore size. The magnitude of the pressure tensor component p_{zz} decreases as the pore size increases from $H = 5$ to $H = 7$. The decrease in pressure tensor indicates the weakening of the induced compression as H increases, consistent with the corresponding decrease of friction force (Fig. 2).

Fig. 2 also indicates that the friction suddenly increases when the pore width increases to 8. The flow characteristics for lubricant molecules inside this pore (Fig. 3c) is the piecewise distribution. For the part near the driving piston, in particular, the internal flow nearly vanishes as a result of solidification, except for the fluid interface layer nearby each confining substrate. The corresponding profile of pressure tensor at $H = 8$ is given in Fig. 4e, which shows the piecewise distribution appears again. Similar to the flow pattern, the pressure distribution for the part of liquid near the driving piston shows the characteristic of solid, but only for molecules in the center of pore. For the liquid layers near the confining substrates, however, the pressure tensor increases gradually along the direction towards the driving piston, showing the liquid-like nature of the contact layers. For the liquid far away from the driving piston, the pressure tensor increases gradually along the direction towards the driving piston, indicating that solidification disappears in this part. What's more, for $H = 8$, p_{zz} near the driving piston is larger than that for $H = 7$. This indicates a stronger compression effect for $H = 8$, leading to an increase in friction (see Fig. 2). Interestingly, this observation also means that molecular clogging might lead to a new kind solid-solid friction with a compressible liquid-like contact layer, which may induce a friction larger

View Article Online
DOI: 10.1039/D6SM00300A

than the solid-solid friction.

For wider pores $H > 8$, Fig. 2 shows that the increase of the pore size monotonously decreases the friction. This tendency can also be deduced from the pressure distribution. As an example, Figure 4f shows the pressure tensor p_{zz} of the liquid slab at $H = 19$. In general, in this case the pressure tensor is basically uniform, and becomes substantially smaller than that of $H = 8$. For such a large pore, p_{zz} is almost constant along Y direction, and the pressure gradient along the wall is rather small, indicating the disappearance of solidification and friction induced-internal compression. This observation originates from the weakened clogging for large pore sizes, and is also the origin of the weakened pore size dependence of the friction force for $H > 19$ (Fig. 2).

In short, the pressure tensor distributions indicate that the interfacial friction produces an internal compression that increases along the direction towards the driving piston. For small pores with a severe clogging effect, the interfacial friction induces a strong increase in the compression along the liquid column, leading to the partial solidification and piecewise pressure distribution. For larger pores, however, the decrease of the clogging effect weakens the internal compression, and accordingly, the piecewise distribution disappears.

Therefore, we interpret the friction/pore size relation as a consequence of the internal compression for the plug-like nanoflow. For sufficiently small pores, the severe clogging induces the superposition of the friction-induced compression, causing a part of the encaged liquid to be locally solidified and leading to the mixture of the liquid/solid friction and the solid/solid friction. Increasing the pore width would generally weaken the clogging effect, leading to the decreases of both the internal pressure and friction force. We also found a special case of partially solidification ($H = 8$), for which the solid-solid friction is featured with compressible liquid-like contact layers.

The partial solidification is also featured with a transition in density distribution and in molecular diffusion. To investigate the friction-induced structural transition of the confined liquid, particularly the partial solidification, we also compare the density distribution with and without the forced friction. Fig. 5 shows that the region where partial solidification takes place features a clearly higher density, when compared to the liquid density. The density increase for solidified fluid is ascribed to the internal compression induced by the combined act of the friction and the clogging effect.

When the liquid slab driven by the piston reaches the steady state, the density profile (see Fig. 5c-f)) along Y axis and Z axis in each individual cell of 1×0.2 is averaged by summing up over 10^5 configurations. As a comparison, the density distribution of the liquid slab without exerting the forced motion is also displayed in Fig. 5a and b. In equilibrium the liquid is uniformly distributed

View Article Online
DOI: 10.1039/D6SM00300A

along the Y axis, while along the Z axis a density peak near the solid substrate appears. The peak corresponds to the layer-like structure for confined liquid near the smooth substrates, and this structure can also be recognized from the pressure tensor profiles (see Fig. 4a andb).

Fig. 5c-f show the density profiles when a constant velocity, $U = 0.015$, is applied. For narrow pore sizes, $H = 5$ and 7 (Fig. 5c and d), the fluid close to the driving piston develops a very high density profile. Specifically, the high density spreads over nearly half of the slab length, and then the density begins to decrease gradually along the Y direction until approaching the free piston. This piecewise density profile confirms the solidification of the confined systems near the driving piston, in agreement with these found in the relative velocity and pressure distributions (Fig. 3 and 4).

For $H = 8$, the density distribution of the liquid slab (Fig. 5e) differs from those for $H = 5$ and $H = 7$: the fluid density of contact layers for $H = 8$ decreases monotonously along the Y axis and the piecewise behavior disappears, a signature that the local liquid layers in contact with the substrates do not solidify for $H = 8$. However, this does not necessarily mean a lower local density. Near the driving piston, the local density for $H = 8$ is in fact larger than that of $H = 7$, because for $H = 7$ the superposition effect vanishes for the solidified part of the encaged liquid. When the pore size further increases, the piecewise structure of the liquid density gradually disappears (see Fig. 5f for $H = 19$) and the density profile is basically the same as the one for the bulk liquid.

In order to verify that the liquid close to the driving piston is solidified when $H = 5\sim7$, we selected five individual chain molecules at five different positions within the pore, and output the variation of their relative position with respect to the driving piston during the simulation time. As shown in Fig. 6, for the three liquid molecules close to the driving piston, their positions relative to the piston remain basically unchanged, indicating that molecules are in a solid-like state; while for other two molecules farther away from the driving piston, their positions fluctuate much more strongly than those near the driving piston, indicating that two molecules are more likely in a liquid state. This again confirms our prediction that the molecules close to the driving piston are in a solid-like state, while these farther away from the driving piston are still in a liquid state.

With the confirmed structures, we can interpret another interesting observation in Fig. 2, namely for cases with $H = 5$ to 7, the friction seems to be velocity independent: when the driving velocity decreases from $U = 0.015$ to 0.0075 the friction is nearly the same for $H < 8$, whereas out of the range, the resulting friction is sensitive to the velocity. This is due to the difference between the liquid/solid friction and the solid/solid friction. For $H < 8$ the local solidification leads to a weakened sensitivity of the solid/solid friction on the applied velocity. For $H > 8$, however, the solidification vanishes. In this situation, as shown in our previous work,[18] the liquid/solid friction between the confined liquid and substrate depends sensitively on the driving

View Article Online
DOI: 10.1039/D6SM00300A

velocity. As the velocity increases, the corresponding liquid/solid friction force increases accordingly.

We note that the partial solidification reported here is a flow-induced phenomenon, not an equilibrium phase transition. It is ease to illustrate that under identical thermodynamic conditions but in the absence of flow, the confined fluid remains entirely liquid, without showing structural signatures of solidification. Only when the driving piston imposes a given velocity, molecular clogging generates a strong internal compression that locally arrests molecular motion, leading to a solid-like region adjacent to the piston. This confirms the non-equilibrium origin of partial solidification.

3.2 The constant force scenario: the solidification inside small pores and solidification-triggered stick-slip transition

To considered different motion mode of the driving piston, we applied the constant force *F* (in reduced units) on the left driving piston along the Y direction, which propels the liquid slab forward. We recorded the position change of the driving piston during the simulation time, and obtained the relationship with the applied force *F* and gained velocity of confined liquid (see Fig. 7a). Based on the simulation results, three distinct types of motion of the liquid slab can be recognized: creep motion, stick-slip motion and interfacial slip motion. Particularly, for the plug-like nanoflow in small pores, we find an abrupt stick-slip transitions as the applied force increases, which results from partial solidification. Whereas in large pores, only continuous transitions is observed because of the absence of solidification.

The creep motion takes place when the force applied to the driving piston fails to overcome the energy barrier required for kinetic friction between confined liquid slab and the solid substrates. Therefore, the driving piston is characterized by extremely slow piston velocity manifesting as creep motion (v<0.001 as shown in the inset of Figure 7a). Meanwhile, the movement of liquid slab is dominated by molecular diffusion, and there is no overall flow observed (see, e.g., Figure 7b for *F*=68 and 146 in the case of *H*=5, and Figure 7d for *F*=79 in the case of *H*=10). During this type of motion, pressure drop concentrates predominantly near the driving piston and near the interfacial layers closest to the solid substrates (Figure 8a and 8b). Whereas, the pressure drop within the bulk fluid region is negligible (Fig. 8a for *F*=68 in the case of *H*=5, and Figure 8b for *F*=79 in the case of *H*=10), showing that molecular motion within the bulk region is primarily governed by diffusion.

We also found the stick-slip transition when the applied force on the driving piston increases. In these cases, the liquid motion gradually transitions from being dominated by internal molecular diffusion to overall flow as the force applied to the driving piston increases. When the force applied exceeds the maximum friction force, thereby enabling the propulsion of liquid slab in rapid forward

View Article Online
DOI: 10.1039/D6SM00300A

motion, leading to a stick-slip transition. Note that we distinguished the creep motion and stick motion according to the pressure distributions (and also density distribution) across the liquid slab: The former is featured with negligible pressure drop along the pore, while the latter is accompanied by the emergence of an significant internal pressure drop along the pore length (Fig. 8a for F=225 in the case of H=5, and Figure 8b for F=900 in the case of H=10). When compared to creep motion, therefore, in stick stage the larger driving force compresses the liquid slab strongly and leads to an increase in forced diffusion-like motion, though the fully developed flow has not yet formed. Once the driving force exceeds the friction force required, interfacial fluid mobilizes, enabling the driving piston to propel the fluid forward in a slip event (see Figure 9 and Fig. 8a for F=2250 in the case of H=5, and Figure 8b for F=1800 in the case of H=10)).

Here we need to point out the difference of the stick-slip transition between H=5 and H=10. For the plug-like nanoflow in small pore of H=5, we find an abrupt stick-slip transitions as the applied force increases. Whereas in the large pore of H=10, continuous stick-slip transitions is observed. The difference is ascribed to the presence/absence of partial solidification (see the pressure tensor and density profiles in Figure 8). When the pore size is small (H=5), the molecular clogging takes place and the liquid slab undergoes partial solidification. The partial solidification is again recognized with piecewise response of the liquid velocity (Figure 9), pressure and density distributions (see Fig. 8a for F=2250). Similarly to the case of constant velocity scenario, the solidification is consequence of the liquid compression induced by interfacial friction (see Figure 7c). The solidification triggers the friction reduction, which resulting in a sudden increase in the liquid slab velocity (Figure 7a). For the pore of H=10, however, no solidification is observed from the velocity distribution (Figure 9) and the pressure tensor distribution (Figure 8b). In agreement with the constant velocity scenario, in such large pore a stable internal flow structure, namely two loops of the friction-driven circulations, is formed (Figure 9).

The third type of plug-like nanoflow corresponds to the interfacial slip motion after the stick-slip transition. In this case, the liquid slab exhibits pronounced interfacial slip behavior: the pressure drop across the interfacial layer decreases, while that within the bulk fluid increases. Consequently, the frictional resistance of the liquid slab shows weak velocity dependence (Figure 7a). As a result, when the driving force continuously increases the friction force remains nearly constant or rises only slightly, whereas the velocity of the liquid column increases sharply.

4 Conclusions

For lubrication at the nanoscale, the friction properties of confined liquids are strongly dependent on the structure of lubricant molecules, but how lubricant molecules organize under strong confinement remains unclear. Here we have focused on the particular region of liquid lubrication called mixed lubrication. The key feature of mixed lubrication is that both

View Article Online
DOI: 10.1039/D6SM00300A

hydrodynamic lubrication and asperity (solid-solid) contacts have to be present simultaneously. At the nanoscale, this scenario can be effectively modeled in terms of a plug-like nanoflow, in which the solid-solid contact can be modelled as a driving piston. In this work, we use molecular dynamics simulations to reveal that plug-like nanoflow under strong confinement can induce partial solidification of the confined fluid, namely a transition from a liquid-like to a solid-like state in the region adjacent to the driving piston. This phenomenon arises from molecular clogging, which amplifies interfacial friction and generates internal compression within the liquid slab. Partial solidification directly leads to a non-monotonic relationship between friction force and pore size.

In our cases, the clogging effect is a joint consequence of the confinement and the presence of the pistons, both of which suppresses the ability of fluid to flow, cooperatively hinder the internal motion of the liquid and enhance the friction on solid interfaces. Our results also suggest that molecular clogging serves as the mechanistic bridge between confinement and solidification: it amplifies the effect of interfacial friction, leading to internal compression that triggers a local solidification. This framework distinguishes molecular clogging from equilibrium jamming and highlights its central role in nonlinear nanofluidic friction.

We then demonstrate that the driving mode fundamentally alters the response of the system. Under constant-velocity driving mode, stable partial solidification in small pores produces piecewise velocity, pressure, and density profiles, and explains the non-monotonic friction. Under constant-force driving mode, three distinct types of motion can be recognized: creep motion, stick-slip motion and interfacial slip motion. Although the two different driving modes show different behaviors, the difference can be interpreted by the same mechanism, namely molecular clogging transforms confined fluids into non-fluidic solids under nanoscale plug flow. It is the partial solidification that triggers abrupt stick-slip transitions in small pores, whereas in larger pores, continuous transitions and stable circulation patterns prevail.

Therefore, we establish a compression-based mechanism linking interfacial friction, molecular clogging, and structural reorganization. Our results show that when confinement shrinks to a few molecular layers ($\approx$1–2 nm), continuum hydrodynamics fails, and solid-liquid phase transitions emerge. Notably, the critical pore size for partial solidification in our model is comparable to the ~1.6 nm liquid-solid transition observed for nanoconfined water at room temperature[33], suggesting a common origin: confinement-induced suppression of molecular entropy. This work provides a mechanistic framework for understanding and predicting nonlinear friction in nanoconfined fluids.

A natural question is whether an effective continuum-level model could capture the nonlinear friction in nanoconfined fluids observed here. Classical hydrodynamics (e.g., the Navier–Stokes

View Article Online
DOI: 10.1039/D6SM00300A

equations) assumes local equilibrium and scale separation, and thus fails to predict the spontaneous emergence of a solid-like region under flow. However, one might consider generalized continuum approaches, via shear-thickening models to mimic the drastic increase in effective viscosity upon strong compression, or alternatively via stress gradient-dependent viscosity to induce a clogged region. However, such a continuum model could not explain why clogging and solidification occur. The solidification mechanism found in this work, namely molecular clogging amplifies interfacial friction, leading to internal compression and a dynamical arrest, remains intrinsically microscopic.

Author contributions

Shan Chen: Formal analysis (equal); Investigation (equal); Writing-original draft (equal); Writing-review & editing (equal); Funding acquisition (equal). Hongguang Zhang: Formal analysis (equal); Investigation (equal); Writing-review & editing (equal); Funding acquisition (equal). Zhenjiang Guo: Formal analysis (equal); Investigation (equal). Ignacio Pagonabarraga: Conceptualization (equal); Supervision (equal); Funding acquisition (equal); Writing-review & editing (supporting). Xianren Zhang: Conceptualization (equal); Funding acquisition (equal); Supervision (equal); Writing-review & editing (supporting).

Conflicts of interest

The authors declare no competing financial interest.

Acknowledgements

We gratefully acknowledge financial support by the Natural Science Research Key Projects of Anhui Province Universities (grant no. 2024AH051310 and 2023AH052272) and Scientific Research Start-up Funds of Bozhou University (grant no. BYKQ202228). We gratefully acknowledge financial support by the National Natural Science Foundation of China (grant no. 22309007 and 22278013). We gratefully acknowledge financial support by the Ministerio de Ciencia e Innovación MCICIN/AEI/FEDER under grant agreement PID2021-126570NB-100 AEI/FEDER-EU, from Generalitat de Catalunya under Program Icrea Acadèmia and project 2021SGR-673.

Data availability statement

The data that support the findings of this study are available from the corresponding author upon reasonable request.

Notes and references

View Article Online
DOI: 10.1039/D6SM00300A

1 Y. Cui, L. Gao, C. Ying, J. Tian and Z. Liu, ACS Nano, 2025, **19**, 1911-1943.

2 X. Yu and W. Ren, *Adv. Funct. Mater.*, 2024, **34**, 2313968.

3 J. Wang, H. Zhou, S. Li and L. Wang, *Angew. Chem. Int. Ed.*, 2023, **62**, e202218321.

4 R. Kumar, A. B. Ghosh, B. Borah, R. Lakkaraju and A. Atta, *Microfluid. Nanofluid.*, 2024, **28**, 74.

5 Y. Meng, J. Xu, Z. Jin, B. Prakash and Y. Hu, *Friction*, 2020, **8**, 221-300.

6 L. Chen and L. Qian, *Friction*, 2021, **9**, 1-28.

7 J. Luo, M. Liu and L. Ma, *Nano Energy*, 2021, **86**, 106092.

8 I. Rosenhek-Goldian, N. Kampf, A. Yeredor and J. Klein, *P. Natl. Acad. Sci.*, 2015, **112**, 7117-7122.

9 J, N. Israelachvili, *Academic press*, 2011.

10 J. Klein and E. Kumacheva, *Science*, 1995, **269**, 816-819.

11 J. Klein and E. Kumacheva, *J. Chem. Phys.*, 1998, **108**, 6996-7009.

12 A. L. Demirel and S. Granick, *Phys. Rev. Lett.*, 1996, **77**, 2261.

13 J. N. Israelachvili, P. M. McGuiggan and A. M. Homola, *Science*, 1988, **240**, 189-191.

14 M. L. Gee, P. M. McGuiggan and J. N. Israelachvili, *J. Chem. Phys.*, 1990, **93**, 1895.

15 H. Yoshizawa and J. Israelachvili, *J. Chem. Phys.*, 1993, **97**, 11300-11313.

16 X. Li, J. Zhang, L. Gong and H. Zeng. *Soft Matter*, 2020, **16**, 6697-6719.

17 D. F. Kienle and T. L. Kuhl, *Phys. Rev. Lett.*, 2016, **117**, 036101.

18 M. A. Smith, E. J. Hallett and S. Perkin, *P. Natl. Acad. Sci.*, 2019, **116**, 25418-25423.

19 Y. Lei and Y. Leng, *Phys. Rev. Lett.*, 2011, **107**, 147801.

20 R. Xu and Y. Leng, *P. Natl. Acad. Sci.*, 2018, **115**, 6560-6565.

21 M. Barisik and A. Beskok, *Microfluid. Nanofluid.*, 2011, **11**, 269-282.

22 S. Chen, Z. Guo, H. Zhang, I. Pagonabarraga and X. Zhang, *Eur. Phys. J. E*, 2022, **45**, 60.

23 S. Plimpton, *J. Comput. Phys.*, 1995, **117**, 1-19.

24 H. R. Warner, *Ind. Eng. Chem. Res.*, 1972, **11**, 379-387.

25 K.Kremer, G. S. Grest, J. Chem. Phys. 1990, 92, 5057.

26 K.Kroger, S. Hess, Phys. Rev. Lett. 2000, 85, 1128.

27 K.Cifre J G H, Hess S, Kröger M. Macromolecular theory and simulations, 2004, 13, 748-753.

28 G. Maitland, M. Rigby, E. Smith, W. Wakeham and D. Henderson, *Oxford University Press*, 1981.

29 M. P. Allen and D. J. Tildesley, *Oxford university press*, 2017.

View Article Online
DOI: 10.1039/D6SM00300A

30 S. Nosé, *J. chem. Phys.*, 1984, **81**, 511-519.

31 W. G. Hoover, *Phys. Rev. A*, 1985, **31**, 1695.

32 K. Shi, J. Chem. Phys., 2023, 158, 040901.

33 W. Zheng, Nature Materials, 2026, 25, 495–501.

View Article Online
DOI: 10.1039/D6SM00300A

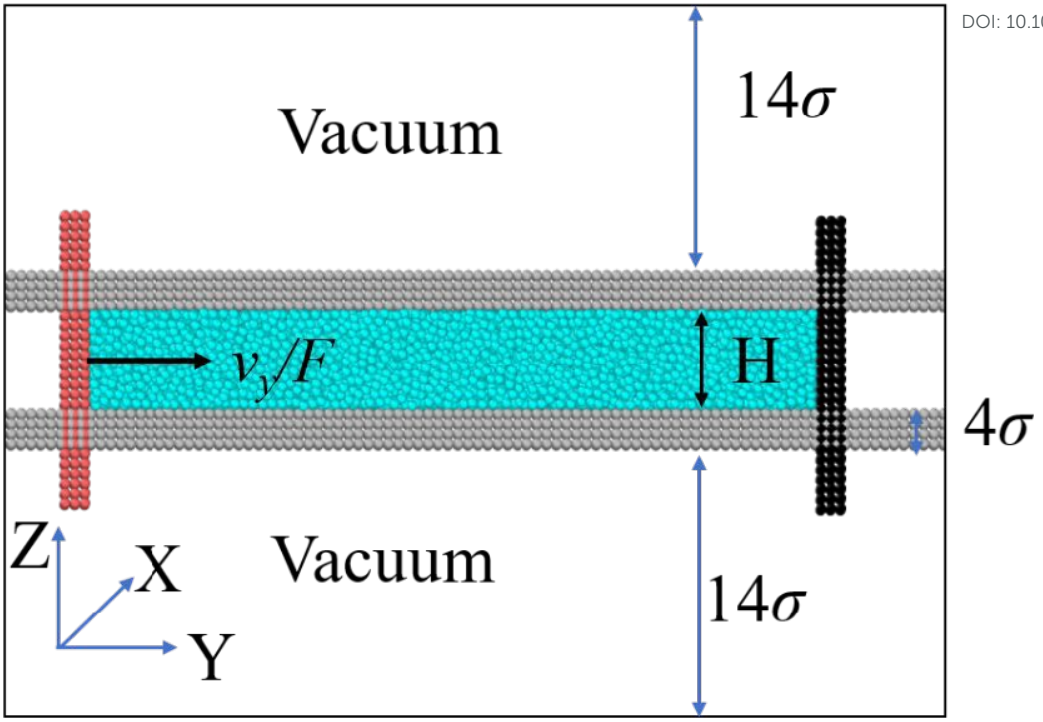

Fig. 1 A typical initial configuration for confined fluid. The upper and lower solid substrates made of four layers of solid atoms confine the liquid (lubricant), while two pistons are placed on both ends of the liquid slab. By applied constant velocity or force on the driving piston (in red), on the left of the liquid slab, provides the driving force for the plug-like flow, while the freely movable piston (in black), on the right, is introduced to eliminate the capillary force. Note that in this work the origin is located at the lower left corner of the simulation box.

View Article Online
DOI: 10.1039/D6SM00300A

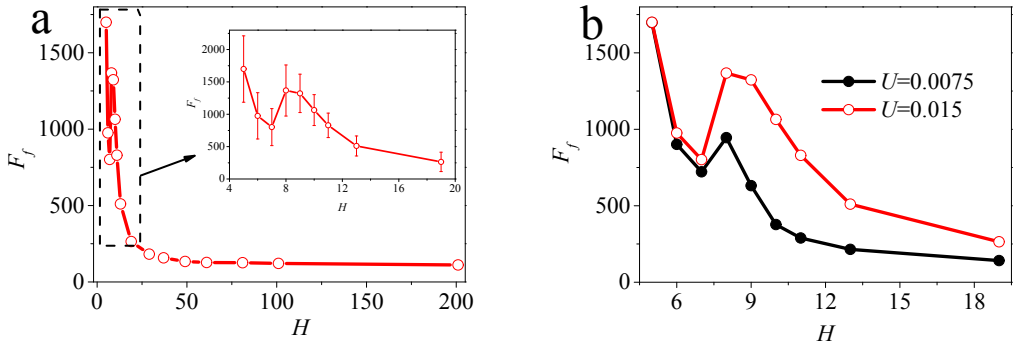

Fig. 2 (a) Friction force shows a non-monotonous relationship with the pore size at fixed piston velocity, $U = 0.015$. (b) Comparison of the induced friction at different driving piston velocities.

View Article Online
DOI: 10.1039/D6SM00300A

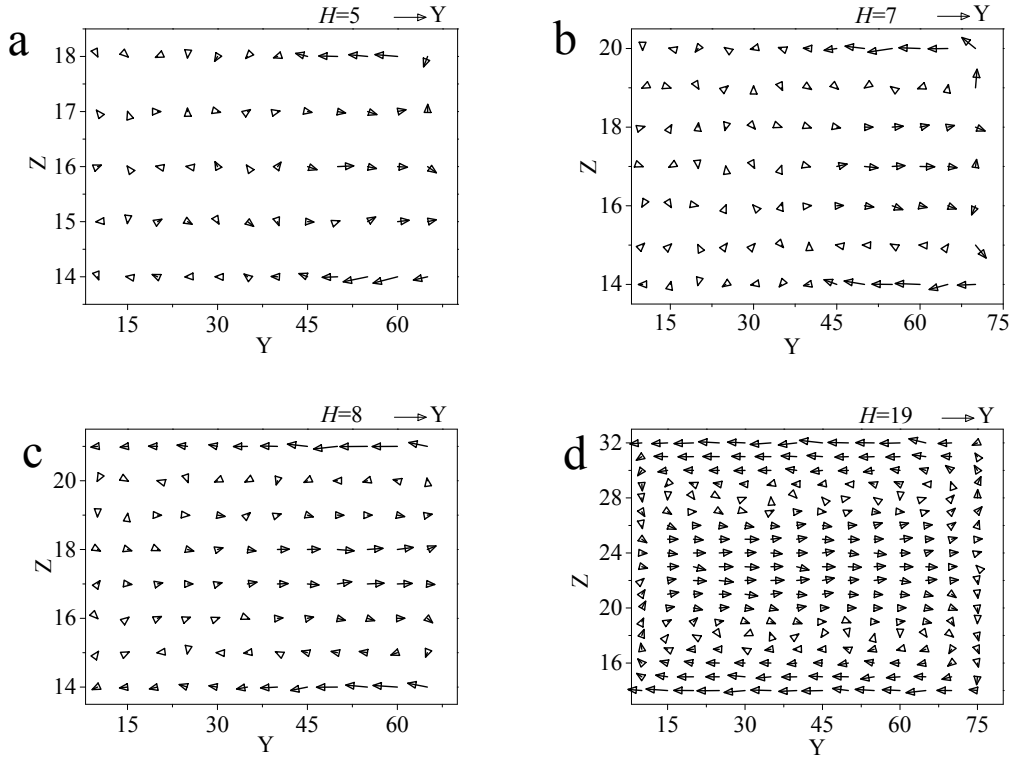

Fig. 3 Relative velocity profile (with respect to the driving piston) for liquid slabs in different pores (a-d): $H = 5$ (a); $H = 7$ (b); $H = 8$ (c); $H = 19$ (d). Here y denotes the relative position of each small cell with respect to the position of the driving piston.

View Article Online
DOI: 10.1039/D6SM00300A

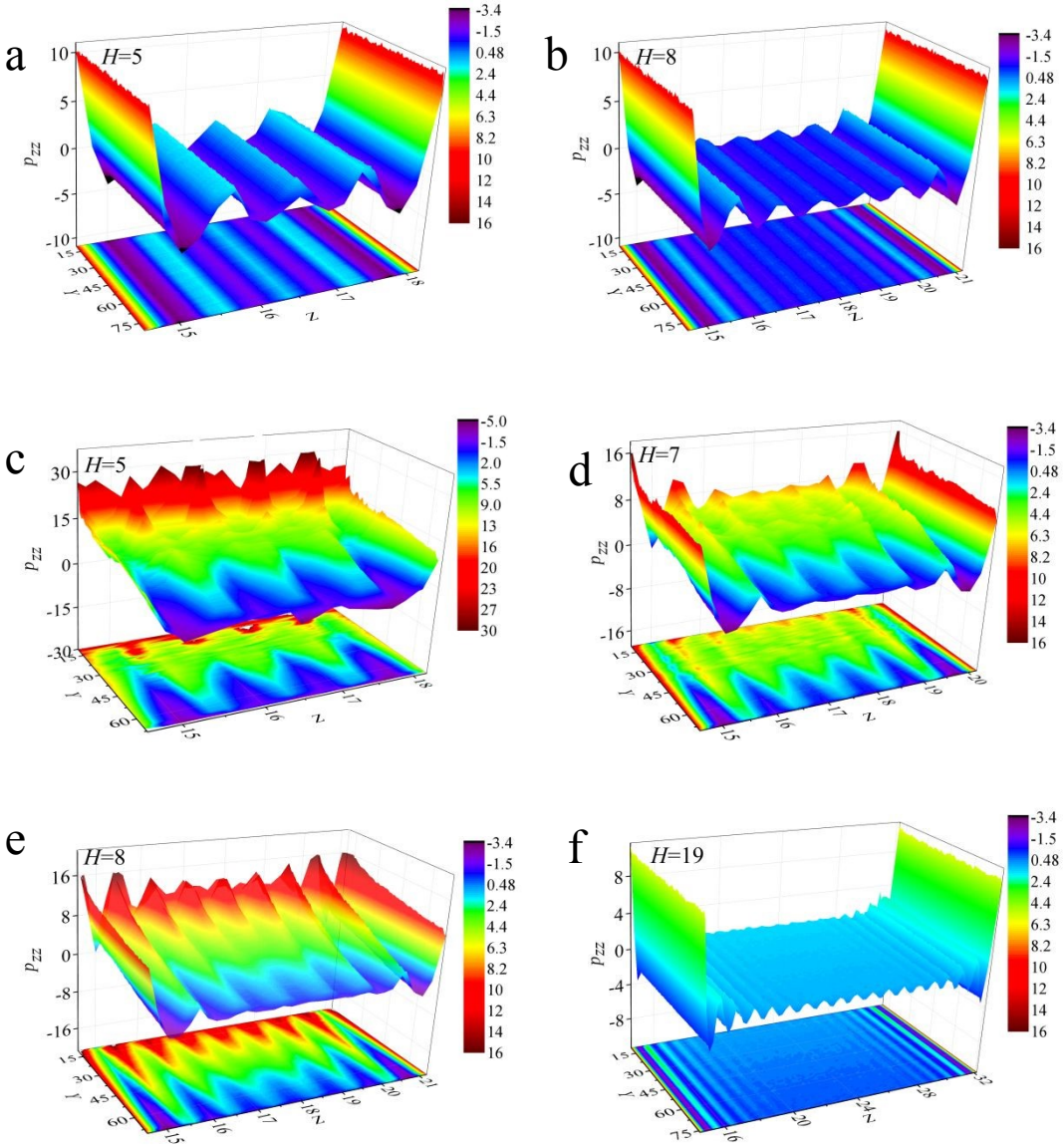

Fig. 4 (a, b) The pressure tensor profile along the *Z* axis, p_{zz}, for the equilibrium state of the liquid slab (without applying a driving velocity): (a) $H = 5$ and (b) $H = 8$. (c-f) The pressure profile of p_{zz} after a constant velocity, $U = 0.015$, is applied by the left piston, with the corresponding pore width: (c) 5, (d) 7, (e) 8 and (f) 19. Here y denotes the relative position of each small cell with respect to the position of the driving piston.

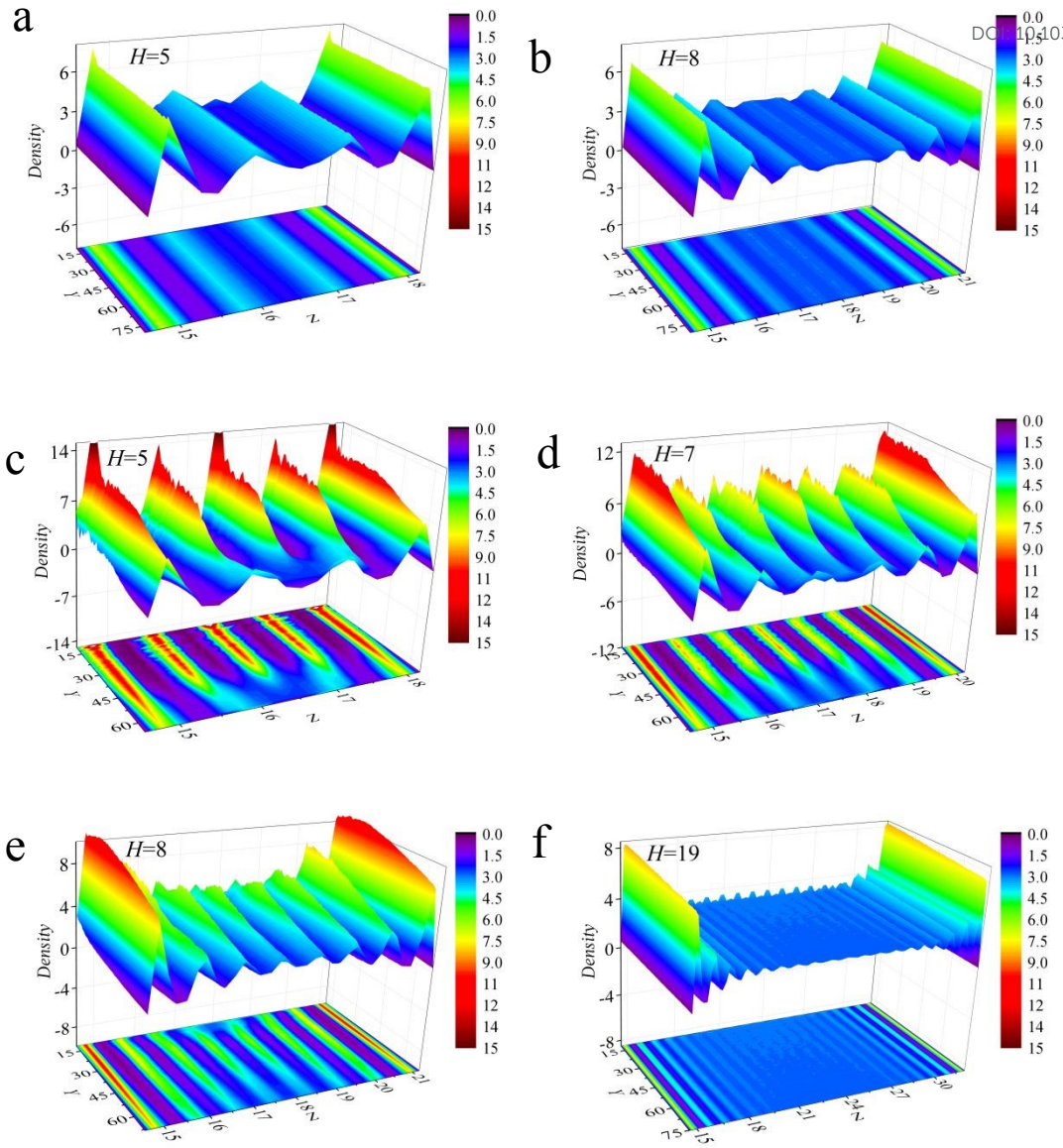

Fig. 5 (a, b) The density profile for the equilibrium state of the liquid slab (without applying the driving velocity: (a) $H = 5$ and (b) $H = 8$. (c-f)). The density profile after a constant velocity 0.015 was applied by the left piston, with the corresponding pore width H: (c) 5, (d) 7, (e) 8 and (f) 19. Here y denotes the relative position of each small cell with respect to the position of the driving piston.

View Article Online
DOI: 10.1039/D6SM00300A

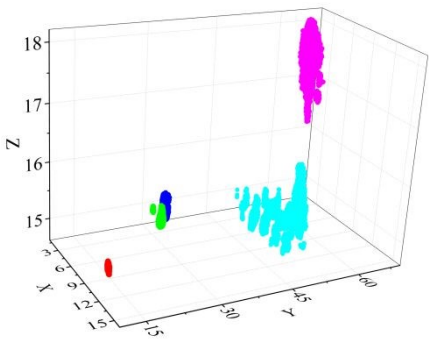

Fig. 6 The relative motion for 5 individual liquid molecules with respect to the driving piston, each indicated by difference colors, during a simulation time of 32ns. In this figure we set H=5.

View Article Online
DOI: 10.1039/D6SM00300A

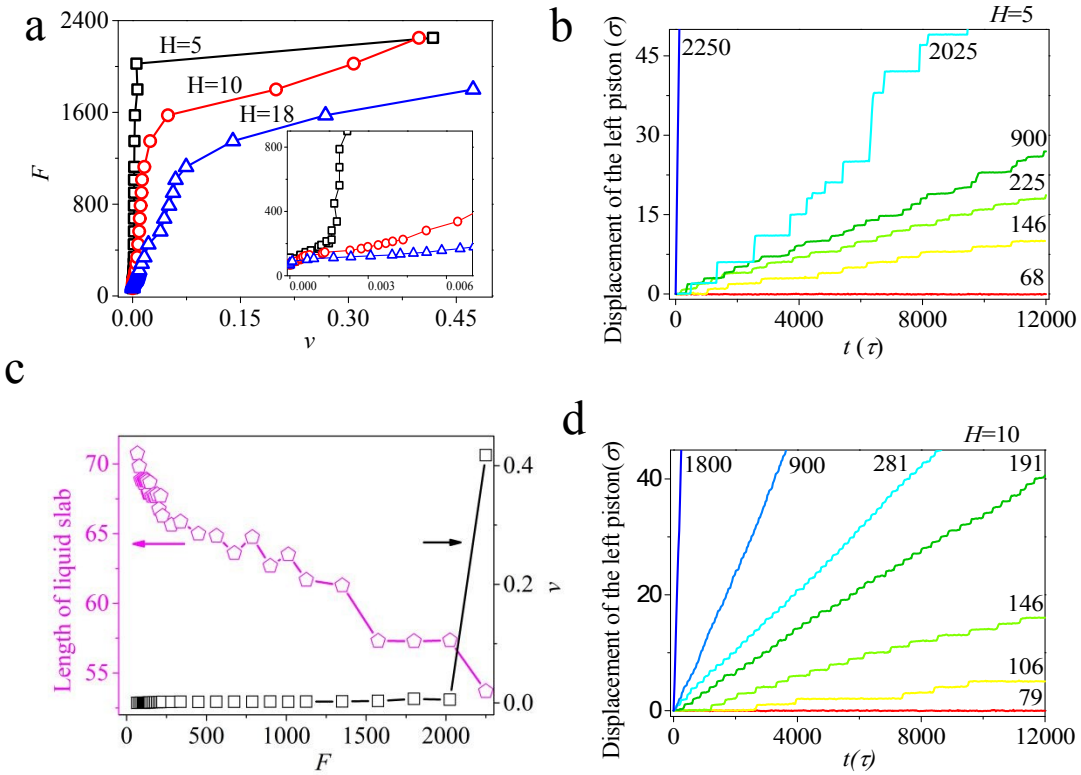

Fig. 7 (a) The relationship between the driving force on the left piston and the averaged velocity within the simulation time. (b and d) show the position displacement of the driving piston(with respect to the initial location) is a function of simulation time for the case of *H*=5(b) and *H*=10(d). The numbers in both figures represent the driving force exerted. (c) The length of liquid slab and velocity change with the applied force on the driving piston.

View Article Online
DOI: 10.1039/D6SM00300A

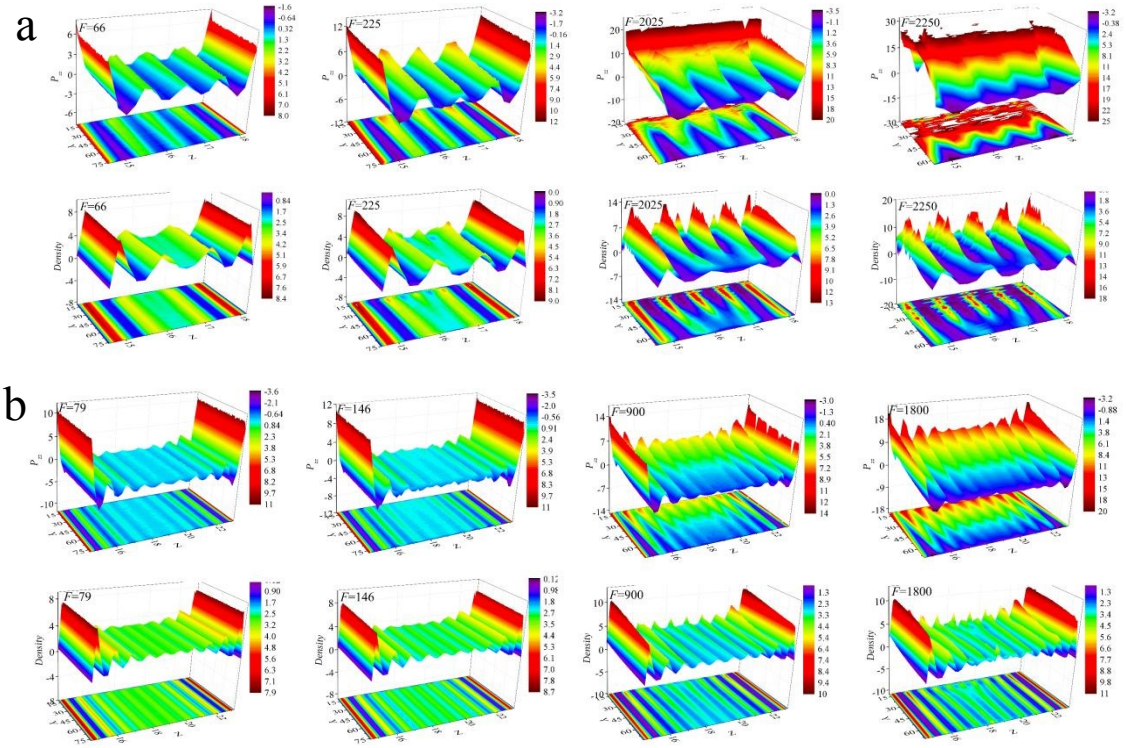

Fig. 8 display the corresponding pressure tensor and density profiles for H = 5 (a) and H = 10 (b), respectively, at several typical values of exerted forces.

View Article Online
DOI: 10.1039/D6SM00300A

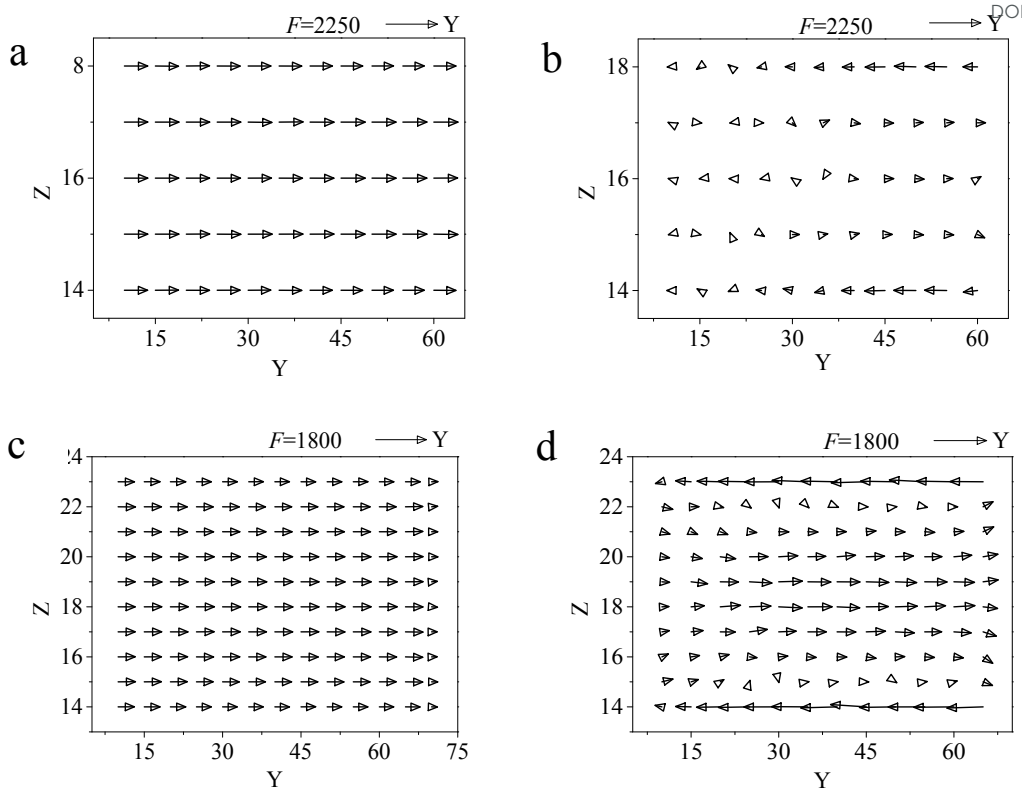

Fig. 9 The flow patterns formed for the slip motion: (a, b) the velocity profile (a) and relative velocity profile (b) at *F*= 2250 inside the pore of *H*=5; (c, d) the velocity profile (c) and relative velocity profile (d) at *F*= 1800 inside the pore of *H*=10.

View Article Online
DOI: 10.1039/D6SM00300A

Data availability statement

The data that support the findings of this study are available from the corresponding author upon reasonable request.